Journal of the Iranian Chemical Society (2024) 21:699–718
https://doi.org/10.1007/s13738-023-02952-1

Functionalized gold nanorods turn-on chemosensor for selective detection of Cd^{2+} ions, bio-imaging, and antineoplastic evaluations

Marwa N. El-Nahass[1] · Eman A. Bakr[1] · Tarek A. Fayed[1] · Wafaa M. Hamada[1] · Maha M. Salem[2] · Aliaa M. Radwan[2]

Received: 22 July 2023 / Accepted: 1 December 2023 / Published online: 27 December 2023

Abstract
A colorimetric turn-on chemosensor based on gold nanorods, Au NRs, has been developed to enable rapid, facile, and simultaneous detection of hazardous metal ions. This study involved the functionalization of gold nanorods with (9,10-dioxo-9,10-dihydro-anthracen-1-yl)-dithiocarbamic acid (DTAD) through the utilization of synthetic photo-irradiation and ultrasound techniques. Various spectroscopic methods were employed to characterize both the synthesized gold nanorods and the chemosensor. The optical response of this sensor was investigated with respect to a range of metal ions, including Mg^{2+}, K^{+}, Ca^{2+}, Mn^{2+}, Fe^{3+}, Co^{2+}, Ni^{2+}, Cu^{2+}, Zn^{2+}, Cd^{2+}, and Pb^{2+}. The results reveal that the DTAD-functionalized gold nanorods chemosensor effectively discriminates all the investigated metal ions, with Cd^{2+} ions exhibiting higher sensitivity and selectivity compared to the other metal ions. Moreover, the anticancer impact of both gold nanorods and DTAD-functionalized gold nanorods was investigated on a panel of cell lines as breast cancer (MCF-7), liver cancer (HepG-2), and colon cancer (Caco-2) using MTT assay. Further, the morphological features and Annexin V using flow cytometry were carried. Comparative analysis with a free chemosensor showed that fluorescence images of living cells were notably brighter in the presence of Cd^{2+}, highlighting the efficacy of DTAD-functionalized gold nanorods as a fluorescent biosensor for Cd^{2+} ions. Additionally, the in vitro anticancer study showed that gold nanorods significantly inhibited the growth of all cancer cells than DTAD-functionalized gold nanorods with best antiproliferative effect on HepG-2 hepatocellular carcinoma with IC_{50} values equal to 1.971 ± 1.28, 40.95 ± 2.56 µg/mL, respectively, compared to DOX. Also, the alteration in the HepG-2 morphological shape and Annexin V results confirmed the great antineoplastic effect of Au NRs than DTAD-Au NRs.

Keywords Chemosensor · Functionalized gold nanoparticles · Cd^{2+} sensing · Fluorescence imaging · Apoptosis

Introduction

Owing to their distinctive optical and electrical characteristics, gold nanorods (Au NRs) have garnered considerable attention, primarily attributed to their shape and dimensions. The confinement of electrons on the surface of gold nanorods engenders shape- and size-dependent features that are not observable in bulk particles [1, 2]. In brief, the formation of plasmon resonances on the surface of respectable metal nanoparticles like gold nanorods allows them to absorb light of different wavelengths. The collective oscillations of the electrons surrounding the nanoparticles are represented by these plasmons. These surface plasmon resonances (SPR) exhibit extremely shape- and size-dependent intensity and wavelength [3–5]. Gold nanorods exhibit two distinct SPR depending on their width and length, known as the transverse and longitudinal plasmon groups (LSPR), because of their anisotropic form. While the LSPR varies significantly depending on the number of nanorods and the overall size, the TSPR is discovered at a fair distance over 500 nm. It is possible to create single-crystalline gold nanorods with LSPR anywhere from the visible to the near-IR region of the electromagnetic spectrum by careful synthesis. Due to the low absorption of surrounding tissue in this region and the capacity of nanorods to absorb NIR light, these materials are suitable for use in biomedical applications [6–8].

✉ Marwa N. El-Nahass
marwa.elnahas@science.tanta.edu.eg

✉ Eman A. Bakr
eman.bakr@science.tanta.edu.eg

[1] Department of Chemistry, Faculty of Science, Tanta University, Tanta 31527, Egypt

[2] Biochemistry Division, Department of Chemistry, Faculty of Science, Tanta University, Tanta 31527, Egypt

However, functionalizing gold nanorods can be notably challenging due to their unique surfactant coating present during their initial synthesis. Typically, cetyltrimethylammonium bromide (CTAB), which strongly adheres to the nanorod surface, is employed during the creation of gold nanorods. Aggravating the CTAB layer can lead to partial or complete aggregation during functionalization, resulting in the loss of desired optical properties.

Heavy metal contaminants in water, given their toxicity, bioaccumulation potential, and persistence, pose a significant threat to both human health and the environment, even at low concentrations [9, 10]. Furthermore, they are challenging to remove from natural and engineered water systems [11]. Various analytical methods, including inductively coupled plasma mass spectrometry, inductively coupled plasma-atomic emission, graphite furnace atomic absorption spectrometry, and fluorescence spectroscopy, are used for the detection and quantification of heavy metals in environmental and biological samples [12–14]. Nevertheless, the cost and complexity of these approaches hinder their use for timely investigations of metal ions. Therefore, the development of user-friendly, cost-effective, selective, and sensitive technologies remains essential to meet environmental requirements and enable on-site real-time monitoring of heavy metals [14, 15]. In our laboratory, we have focused on developing simple and affordable fluorescent probes for the sensing of toxic metal ions due to their high sensitivity even at low concentrations. Essential metal ions for human health, such as Mg^{2+}, K^{+}, Ca^{2+}, Mn^{2+}, Fe^{3+}, Co^{2+}, Ni^{2+}, Cu^{2+}, Hg^{2+}, Zn^{2+}, and Pb^{2+}, are included in the metal ion detection repertoire [16–20].

Gold nanorods-based colorimetric assays have long been of significant interest because they can selectively and sensitively detect a wide array of chemical species without the need for complex procedures, thanks to the remarkably high extinction coefficients of gold nanoparticles in the visible spectrum, which are distance-dependent optical properties [21].

Furthermore, gold nanoparticles have found extensive utility in various biological applications, including photothermal therapy and drug delivery, due to their outstanding stability and sensitivity [22]. Given the substantial global impact of cancer, characterized by high mortality and morbidity rates, the development of effective treatments has become imperative. Nanomaterials offer a potential revolution in cancer detection and treatment [23]. Also, it is important to note that while gold nanoparticles show promise in cancer therapy, more research is needed to fully understand their safety and effectiveness. The field of nanomedicine continues to evolve, with ongoing efforts to develop gold nanoparticles and other nanomaterials into viable treatments for various types of cancer [24].

In this study, we have devised and synthesized a gold nanorods-based colorimetric chemosensor designed for the detection of multiple metal ions, including Mg^{2+}, K^{+}, Ca^{2+}, Mn^{2+}, Fe^{3+}, Co^{2+}, Ni^{2+}, Cu^{2+}, Zn^{2+}, Cd^{2+}, and Pb^{2+} ions. Gold nanorods were functionalized with (9,10-dioxo-9,10-dihydro-anthracen-1-yl)-dithiocarbamic acid, DTAD to enable this application. Substantial enhancements in selectivity and sensitivity have been achieved for specific metal ions. Additionally, the chemosensor facilitated fluorescent imaging of Cd^{2+} particles within living cells. In vitro assessments were also conducted to evaluate the anticancer potential of gold nanorods against various cancer cell types.

Materials and methods

Chemicals

The chemical reagents employed in this study encompassed 1-amino-anthraquinone (AAQ), silver nitrate ($AgNO_3$), hydrogen tetrachloroaurate ($HAuCl_4{\cdot}3H_2O$), magnesium acetate ($Mg(CH_3COO)_2$), potassium chloride (KCl), calcium chloride ($CaCl_2$), manganese chloride tetrahydrate ($MnCl_2{\cdot}4H_2O$), ferric chloride ($FeCl_3$), cobalt chloride hexahydrate ($CoCl_2{\cdot}6H_2O$), nickel chloride hexahydrate ($NiCl_2{\cdot}6H_2O$), copper chloride dihydrate ($CuCl_2{\cdot}2H_2O$), cadmium chloride ($CdCl_2$), zinc sulfate ($ZnSO_4$), lead acetate ($Pb(CH_3COO)_2$), ethanol, carbon disulfide, and sodium chloride. All chemicals were sourced from reputable suppliers, namely Merck-Aldrich and Sigma-Aldrich, USA, and were utilized in their as-received state without additional purification. Double-distilled water served as the solvent for sample preparation and solution formulation.

Synthesis of gold nanorods, Au NRs

For synthesis of Au nanoparticles, a reaction solution containing 80 mM of CTAB, and 2.5 mM of tetrachloroauric acid, $HAuCl_4.\ 3H_2O$, was mixed with 2.5 mL of acetone and 1.7 mL of cyclohexane. After that, 4.0 mL of 10 mM $AgNO_3$ solution was added slowly to the reaction mixture. As a next step, 7.5 mL of 40 mM ascorbic acid (AS) was added to the reaction mixture (total volume = 109.3 mL). Addition of the AS solution results in instantaneous color change from pale yellow to colorless by exposure to UV light (the irradiation source was a UV lamp (model UVL-21, UVP, INC, San Gabriel, California, USA, $\lambda = 365$ nm); this solution was changed to blue.

Beyond the reduction step, UV radiation is essential for the formation of Au NRs because the photons provide the activation energy needed for the nucleation and growth. This is seen by the increase in the rate of Au NR creation when compared to particle generation in the dark.

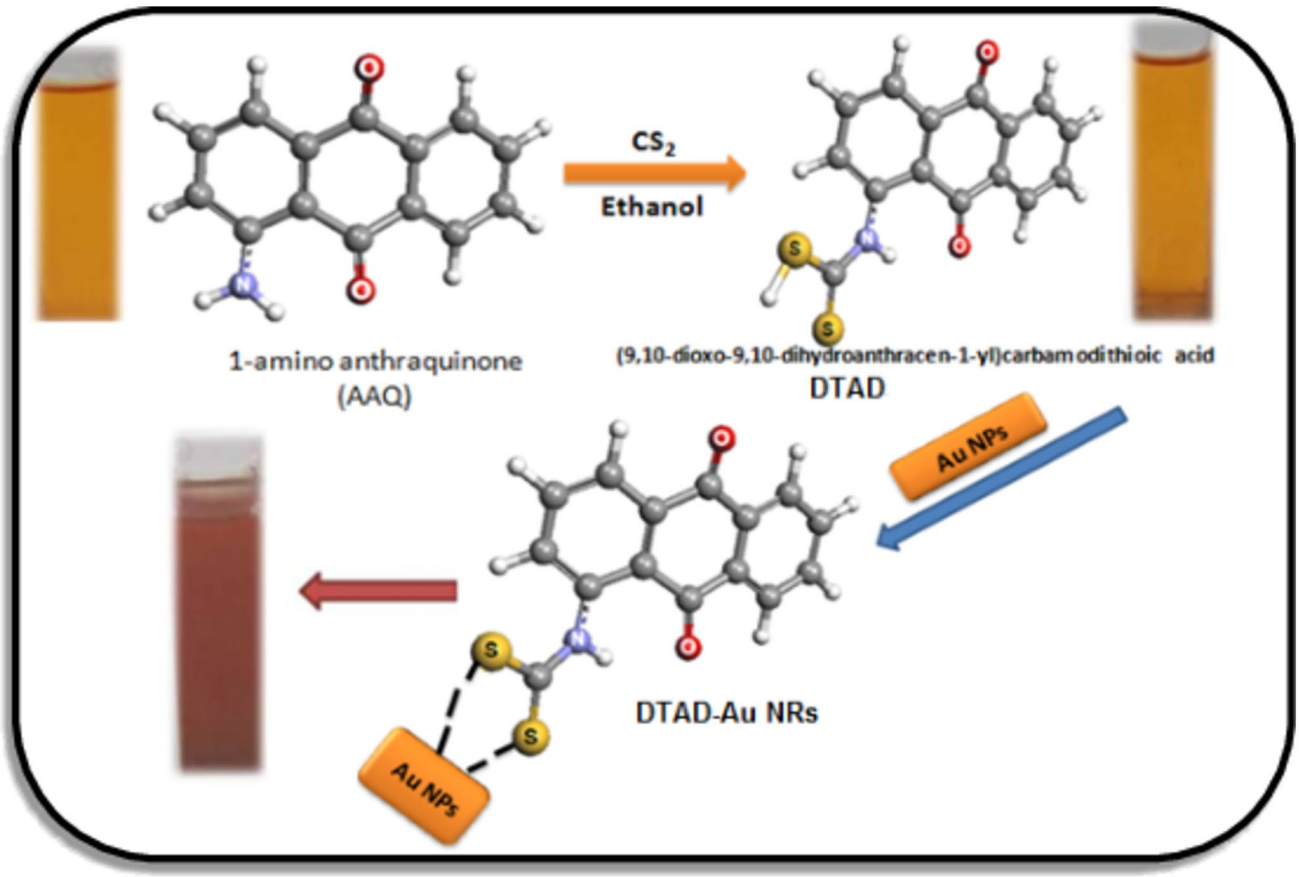

Scheme 1 The synthesis procedures of DTAD and the DTAD-Au NRs chemosensor

Synthesis of DTAD-Au NRs chemosensor

By subjecting 500 M of 1-aminoanthraquinone, AAQ, to an equimolar mixture of ethanolic CS_2 and ultrasonic treatment for one hour, the compound (9,10-dioxo-9,10-dihydroanthracen-1-yl)-dithiocarbamic acid, DTAD, was created [25]. In total, 100 mL of Au NRs was combined with 10 mL of the synthesized DTAD. A reddish-brown solution was produced when the mixture was sonicated for a further hour at room temperature to allow DTAD molecules to self-assemble on the surface of Au NRs. Prior to being used in all experiments, this solution was stored in a refrigerator at 4°C. The production processes for the DTAD and DTAD-Au NRs chemosensors are shown in Scheme 1.

Characterization

FT-IR-4100 (JASCO, Japan) spectrophotometer is used to record the FT-IR spectra using KBr pellets within the range 4000–400 cm^{-1} with a resolution of 2 cm^{-1}.The ^{1}H-NMR spectra were recorded in DMSO using Bruker DPX 200 spectrometer. The morphology was examined by transmission electronic microscopy (TEM) using JEOL (Jem-2100) electron microscope/HT 200 eV/Resolution 0.1432 nm/Option 1.5 million. Zeta potential was measured employing a Brookhaven zeta potential/particle size analyzer. The UV–Vis absorption and emission spectra were recorded utilizing Shimadzu double-beam UV–Vis Scanning (UV-3101 PC) and Agilent Cary Eclipse Fluorescence Spectrophotometers using quartz cuvettes.

Cell probing studies

Fresh peripheral blood was taken with anticoagulants (Heparin). The fresh blood was diluted with equal volume of phosphate buffer saline (PBS) without Ca^{2+} and Mg^{2+} ions. Diluted blood was carefully added over Ficoll in the ratio 2:1 in a 50-mL falcon tube and then centrifuged at 2000 rpm for 25 min. The middle puffy layer was slowly aspirated by a pipette and then evacuated into 50-mL falcon tube followed washing twice by PBS at 1300 rpm for 10 min [26]. The cell pellet was suspended and spread over glass slides and left to dry. Mononuclear cells were settled by absolute cold methanol and then left to dry. The AAQ dye, Au NRs, and DTAD-Au NRs in the presence of Cd^{2+} were included to the cells for 5 min in dark, then washed with distilled water,

and left to dry. Slides were examined under Olympus BX50 fluorescent microscope equipped with Olympus BH2-RFL-T3 mercury vapor lamp as illuminator. Imaging was done utilizing an Olympus camera (c-7070).

In vitro anticancer activity of Au NRs and DTAD-Au NRs

Cell culture

Human colon cancer (Caco), liver cancer (HepG-2), and breast cancer (MCF-7) cells were obtained from Excellence for Research in Regenerative Medicine and Applications Center (Alexandria, Egypt). The cells were cultured and maintained in Dulbecco's modified Eagle's medium (DMEM) supplemented with 10% heat-inactivated fetal bovine serum (Sigma-Aldrich Chemical Co., St. Louis, MO, USA) in humified 5% CO_2 incubator at 37ºC. The cells were passaged every 3 days after confluency [27].

Cell proliferation assay

The cell proliferation was assessed using MTT assay [28]. Briefly, 1×10^4/mL cells were seeded in 96-well plate and incubated for 24 h before treatment. On the next day, the old medium was removed and replaced with fresh one containing different concentrations of Au NRs and DTAD-Au NRs and the cells were incubated in CO_2 incubator. After 48 h, 0.5 mg/mL MTT solution (Sigma-Aldrich Chemical Co., St. Louis, MO, USA) was added to each well and the cells were incubated for further 4h at 37 °C. Finally, MTT solution was replaced with 150 µL DMSO to dissolve the formazan crystals. Microplate reader (Bio-Rad, Hercules, CA, USA) was used to measure the optical density at 570 nm. The concentration of drugs that inhibit 50% of cell growth was then calculated.

Cell morphology assessments

An inverted light microscope (Olympus, USA) was used to observe and capture the morphological changes of apoptotic cells. In brief, 5×10^5 HepG-2 cells were incubated in six-well plate with or without IC_{50} of Au NRs and DTAD-Au NRs for 48 h. Then, the medium was removed, and the cells were washed with PBS. The morphological differences of treated and untreated cells were captured [29].

Apoptosis measurement by flow cytometry

Flow cytometric measurements were taken to assess the cells undergoing early and late apoptosis after incubation with Au NRs and DTAD-Au NRs. HepG-2 cells were seeded in six-well plate at density of 1×10^6/well. After 24h, the cells were treated with IC_{50} of Au NRs and DTAD-Au NRs and incubated at 37 °C for 48 h. Then the cells were harvested and washed with cold PBS. Using an Annexin V-FITC kit (Becton-Dickinson), treated cells were tested for phosphatidylserine exposure according to the manufacturer's instructions. BD FACS Calibur flow cytometer was used for measuring apoptosis in stained cells and Cell Quest™ software for data analysis [30].

Results and discussion

Mechanism of Au NRs Growth

To achieve the development of Au NRs, it is necessary to comprehend the method by which they are produced. This was done by examining the roles that each reactant plays in the creation of Au NRs. The growing procedure for creating Au NRs is shown in detail in Scheme 2.

The cationic surfactant CTAB plays a role in the development of Au NRs because, when dissolved in water at a concentration higher than its critical micelle concentration, it forms micellar or vesicular structures CTA^+ and Br^- ions as shown below:

$$CH_3(CH_2)_{15}N^+(CH_3)_3Br \rightarrow CH_3(CH_2)_{15}N^+(CH_3)_3 + Br^-$$

$$CTAB \rightarrow CTA^+ + Br^-$$

For Au NR to develop, bromide ions must be present as the surfactant counter ion. The CTAB solution undergoes a multi-step ligand exchange when $HAuCl_4$ is introduced, replacing the Cl^- ions with Br^- ions. A crucial part of controlling the mechanism of Au NRs' production is played by silver ions.

$$H^+\left[Au^{III}Cl_4\right]^- + Br^- \rightarrow CTA^+\left[Au^{III}Br_4\right]^- + 4\,Cl^-$$

$$AgNO_3 + Br^- + CAT^+ \rightarrow CTA^+\left[Ag^{I}Br_2\right]^- + NO_3^-$$

A competitive reduction between Au(III) and Ag(I) complexes takes place after ascorbic acid is added to the surfactant-stabilized gold and silver complexes. According to the following equations, $[AuIIIBr_4]^-$ not $[AgIBr_2]^-$ is reduced, which causes the produced yellow-orange color to disappear:

$$CTA^+[Au^{III}Br_4]^- + CTA^+[Ag^{I}Br_2]^- \xrightarrow{AS} CTA^+[Au^{I}Br_2]^- + 2Br^-$$

Strong electrostatic forces between the reduced particles are produced by the positively charged part of the surfactant CTA^+. Due of these electrostatic forces, particles adhere end-to-end rather than side-by-side, which drives the soft

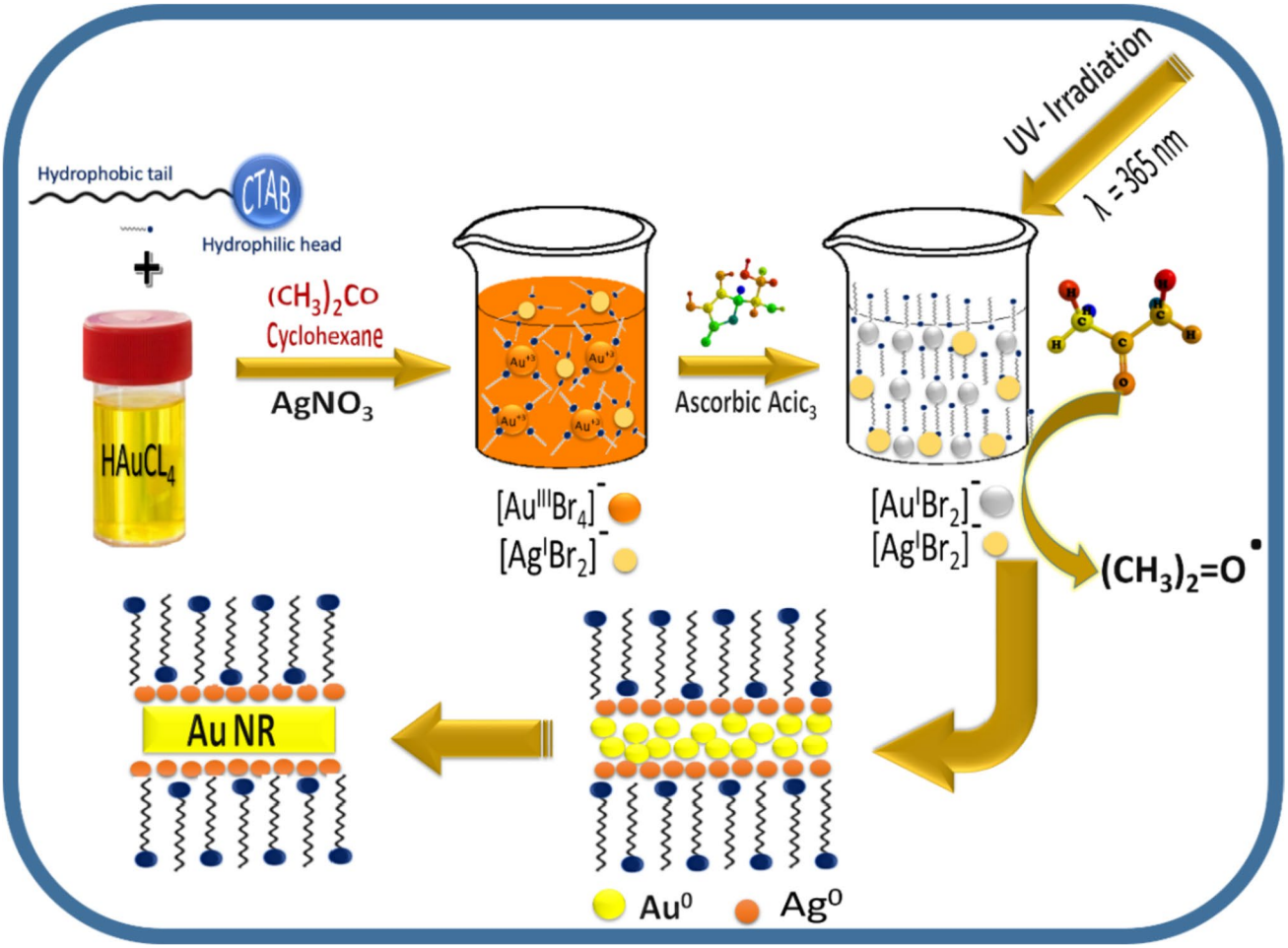

Scheme 2 The mechanism of Au NRs growth

template for developing Au NR particles. Wherein silver's role is to regulate or facilitate the aggregation of the particles before being phase-separated from the resulting Au NRs.

Beyond the reduction step, UV photons are the primary factor in the creation of AuNPs. The activation energy required for the nucleation and growth is provided by the photons. Acetone is thought of as the photoinitiator and the source of the ketyl radicals $R_2C^{\bullet}$ that are produced under UV illumination through its excitation and subsequent hydrogen abstraction from CTA^+ as follows [31]:

$$\left(CH_3\right)_2C=O+h\nu \rightarrow \left(CH_3\right)_2C=O^{*} \text{ Excited acetone}$$

$$\left(CH_3\right)_2C=O^{*}+RH \rightarrow \left(CH_3\right)_2C^{\cdot}-OH+R^{\cdot}$$

where RH and $R^{\bullet}$ denote CTA^+ and its alkyl radical generated by hydrogen abstraction. The generated radicals could be responsible for the reduction of Au^I to Au^0. Also, the presence of cyclohexane is essential for gold nanorod synthesis, where it swells the aliphatic part of the micelles and promotes elongation. Without the use of cyclohexane, anisotropic AuNPs with extremely wide sizes and aspect ratio distributions spontaneously arise throughout the synthesis process [32], while the reduction of Ag^+ ions by microscopic Ag(0) clusters and/or islands should be expected to occur more readily by the uptake of electrons at the surface of the first nucleated Au seeds [33]. Although other writers have suggested that AgBr could develop and be adsorbed onto the surface of Au NP [34]. On the other hand, in the presence of Au(I) species, Ag(0) could reoxidize to Ag [35, 36].

The absorption spectra were recorded after adding all aspects with the observable color changes in order to follow the growth of Au NRs at each stage, as shown in Fig. 1. The yellow color of the aqueous $HAuCl_4.3H_2O$ solution absorbs at 309 nm, as seen in Fig. 1a. A new absorption band at 397 nm with a shoulder around 472 nm has been noticed when $HAuCl_4$ is added to the CTAB solution with the help of acetone, cyclohexane, and $AgNO_3$. The surface plasmon spectra of Ag^0NPs disappear, indicating that Ag^+ ions are not reduced at this stage, and the yellow-orange colored

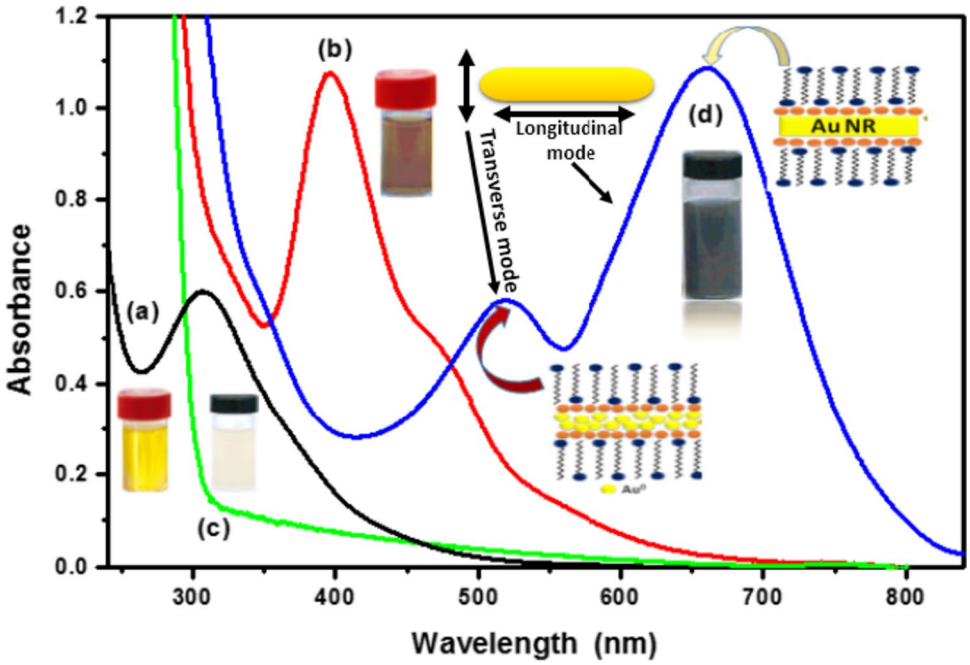

Fig. 1 Absorption spectra of **a** aqueous $HAuCl_4$, **b** solution containing $HAuCl_4.3H_2O$, CTAB, acetone, cyclohexane, and $AgNO_3$ in the absence of ascorbic acid, **c** in the presence of ascorbic acid, **d** the formed Au NRs after 5 min of UV irradiation of solution c. Inset the color changes after each addition

solution becomes colorless after ascorbic acid is added to the surfactant-stabilized gold and silver complexes.

The blue color of the Au NRs was created by exposing the formed solution to a UV lamp for 5 min, as shown in Fig. 1c. Two peaks at 522 and 659 nm may be observed in the Au NRs' absorption spectra. The transverse plasmon band, with its short-wavelength peak at 522 nm, is associated with oscillations parallel to the major axis of the rod, while the longitudinal plasmon band, with its long-wavelength peak at 659 nm, is associated with oscillations along the long axis of the rod. While the longitudinal plasmon band may be shifted to the NIR region as the aspect ratio of the nanorods grows, the transverse plasmon band is rather immune to changes in the aspect ratio of nanorods.

Figure 2 shows UV–Vis absorption spectra of gold nanorods formed with various irradiation times. Two surface

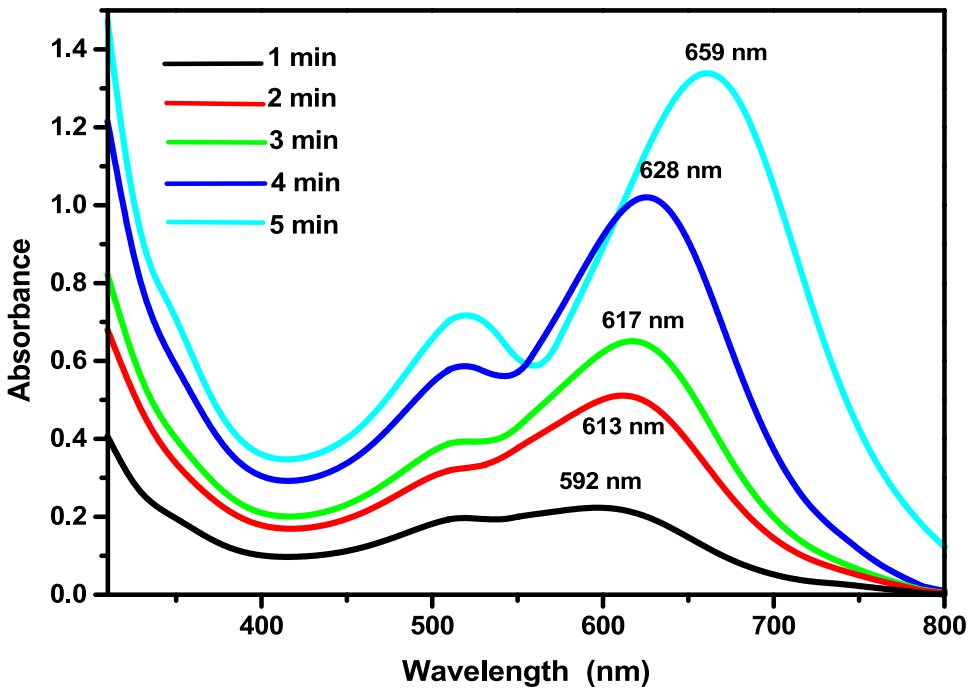

Fig. 2 The effect of irradiation times on the formation of Au NRs

plasmon resonance absorption peaks can be seen in all of the spectra: one at about 522 nm, which corresponds to the transverse electronic oscillation, and the other between 592 and 659 nm, which corresponds to the longitudinal electronic oscillation. This figure illustrates how the position of the transverse electronic oscillation absorption peak is nearly constant, while the longitudinal electronic oscillation absorption peak substantially depends on the irradiation time. The longitudinal electronic oscillation-induced absorption peak is red-shifted from 592 to 659 nm when the irradiation time is increased from 1 to 5 min, indicating the increase in aspect ratio of the nanorods.

Characterization of the investigated materials

^{1}H-NMR Spectra

The ^{1}H-NMR spectra of 1-aminoanthraquinone, AAQ and (9,10-dioxo-9,10-dihydro-anthracen-1-yl)-dithiocarbamic acid, DTAD are shown in Fig. 3. The aromatic protons of AAQ can be identified by the peaks at 7.19 and 8.19 ppm. The proton of the AAQ's -NH_2 group, however, is what makes up the peak at 3.77 ppm. In addition, the broad peak at 4.31 ppm is the result of the integration of DTAD's

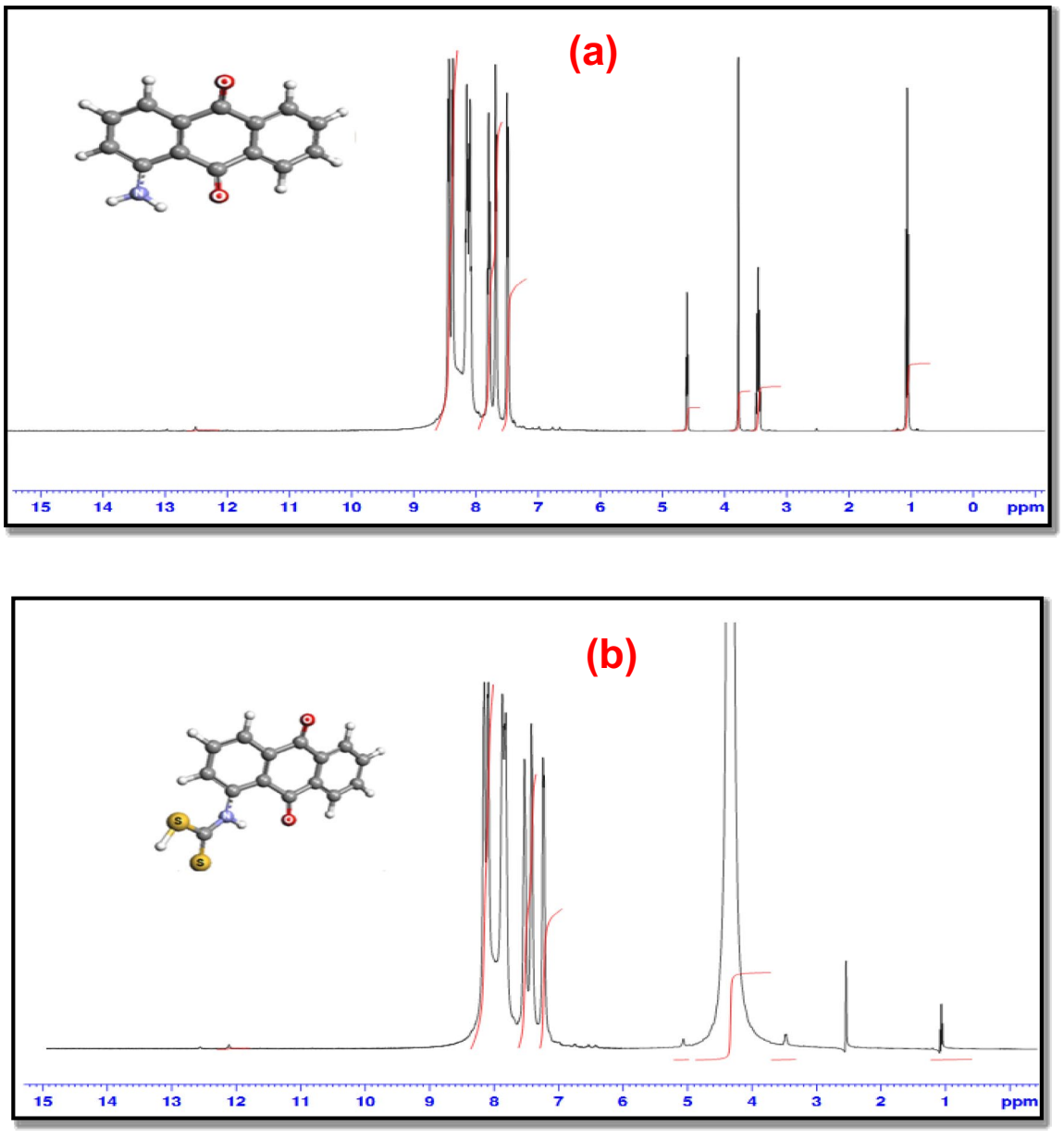

Fig. 3 ^{1}H-NMR spectra of **a** 1-aminoanthraquinone, AAQ, and **b** (9,10-dioxo-9,10-dihydro-anthracen-1-yl)-dithiocarbamic acid, DTAD in DMSO

-NH. Due to the synthesis of DTAD, the new peak that was identified at 2.51 ppm assigned to the –SH group.

FT-IR spectral analysis

The FT-IR spectra of AAQ, DTAD, and the DTAD-Au NRs chemosensor are shown in Fig. 4. Two distinctive bands at 3429 and 3300 cm^{-1}, which correspond to the NH_2 group, may be seen in the FT-IR spectrum of AAQ. The stretching mode of C–N is responsible for the absorption band at 1279 cm^{-1}. The stretching of the aromatic C–H is what causes the band at 709 cm^{-1}. The stretching vibrations of the C=O group are attributed to the band at 1616 cm^{-1}. The FT-IR spectrum of DTAD exhibits new peaks characteristic to the stretching vibrations of C–S, –S–H, –N–H, and CS-NH groups at 1080, 2397, 3423, and 1374 cm^{-1}, respectively. The FT-IR spectrum of DTAD-Au NRs reveals that –S–H group stretching and bending modes are not observed at 2397 cm^{-1} due to the successful attachment of DTAD on the surface of Au NRs via thiolate linkage.

TEM analysis

TEM images of Au NRs and DTAD-Au NRs are shown in Fig. 5a, b. As seen in Fig. 5a, Au NRs contains combinations of particle populations with varied aspect ratios (width to length ratios), primarily nanorods and partially nanocubes. The nanocubes are thought to be artifacts of the synthesis process. But Fig. 5b displays TEM images of DTAD-Au NRs, demonstrating that DTAD molecules are present on Au NRs. The DTAD molecules on Au NRs reduce the effects of the chemical interface on the plasmon resonance, preventing the Au NRs from aggregating, and lowering the surface energy to balance the thermodynamic driving forces. This enables more direct control and effective dispersion of particle size in aqueous media. [25]

Steady-state absorption and emission spectra

The absorption spectra of DTAD, free AAQ dye, and DTAD-Au NRs are displayed in Fig. 6. As can be observed, the presence of CS_2 confirmed the formation of the DTAD compound because the free AAQ dye's absorption spectrum, which was at 489 nm, was red-shifted by 13 nm. The absorption spectra of DTAD-Au NRs, however, are shown in Fig. 6c, where two absorption peaks at 495 and 650 nm were observed.

The stability of DTAD-Au NRs was examined by measuring its absorption spectra over a range of time periods. As seen in Fig. 7, the absorption peak positions of DTAD-Au NRs at 502 and 650 nm were the same from the first to the seventh day, demonstrating that DTAD-Au NRs remain stable for a long time, confirming that the surface modification of Au NRs with DTAD prevents Au NRs aggregation.

Figure 8 displays zeta potential measurements for solutions of Au NRs and DTAD-Au NRs. The spectra for Au NRs and DTAD-Au NRs show negatively charged particles at – 27 and – 40 mV, respectively. The stability of the colloidal dispersions in water is confirmed by these negative findings.

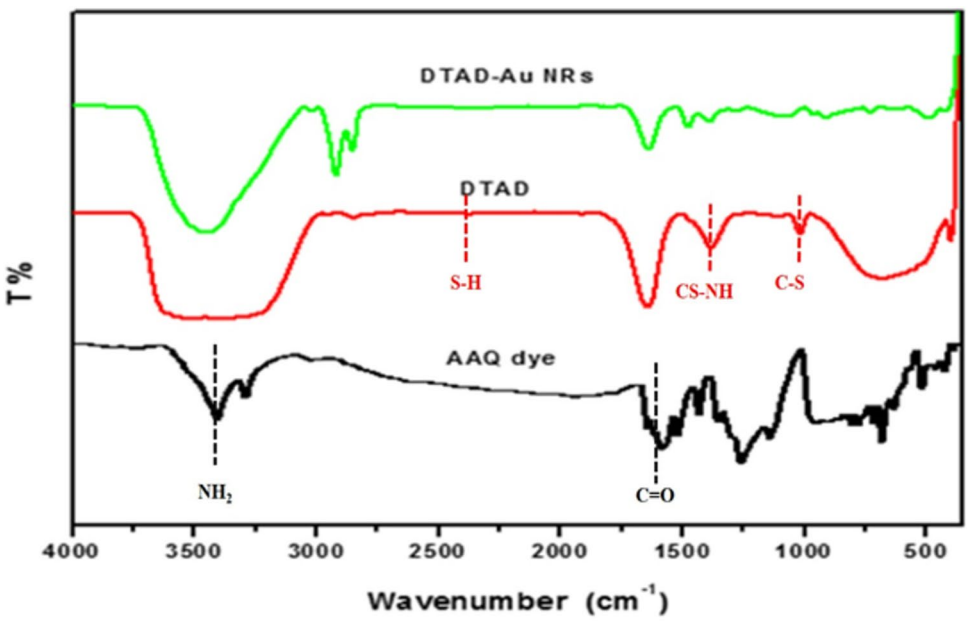

Fig. 4 FT-IR spectra of AAQ, DTAD, and DTAD-Au NRs

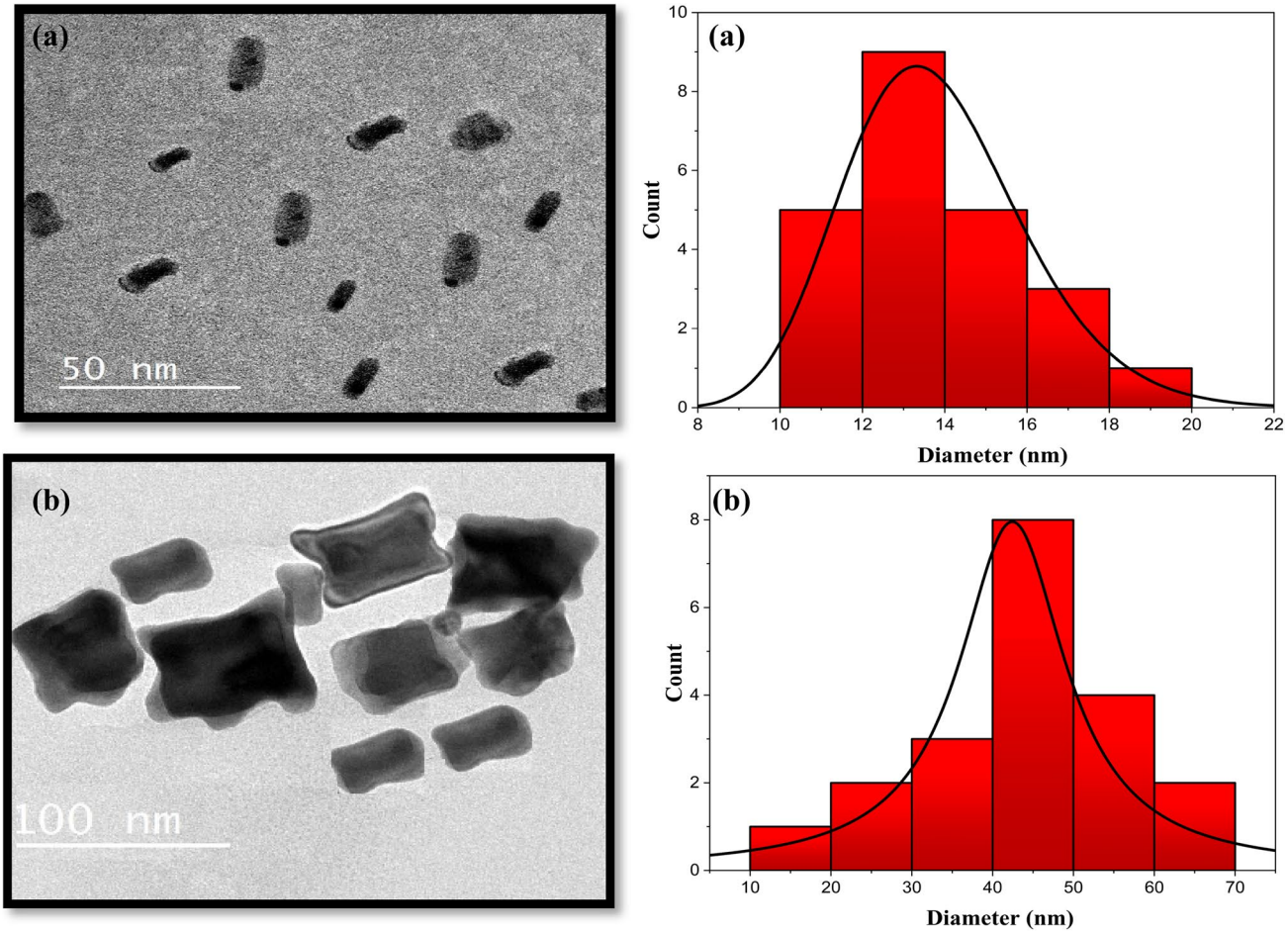

Fig. 5 TEM images and particle size distribution of **a** Au and **b** DTAD-Au NRs

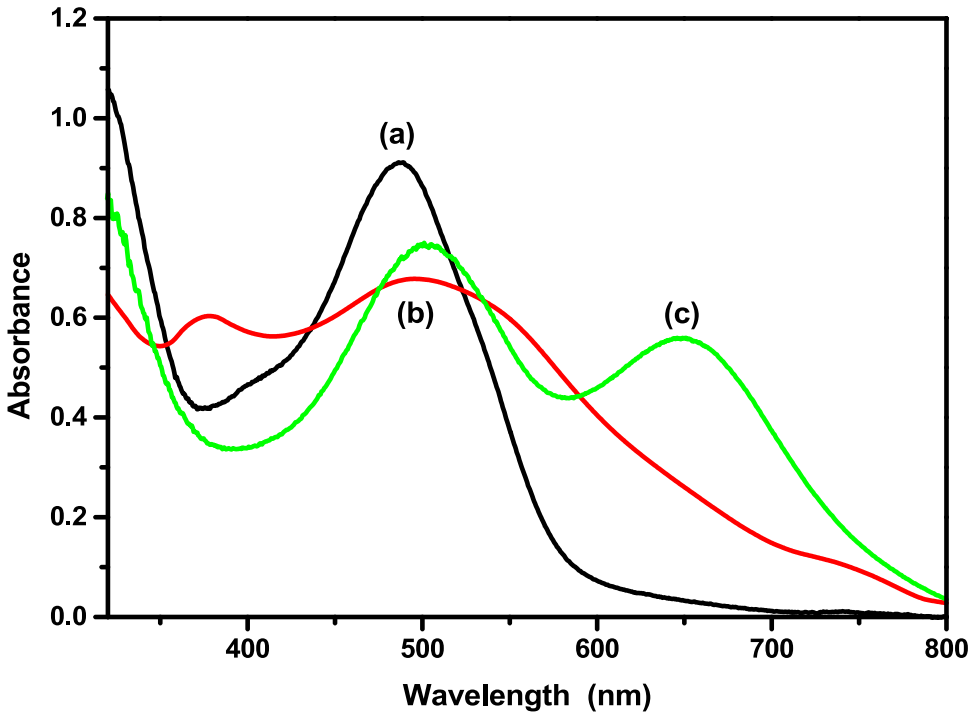

Fig. 6 Absorption spectra of **a** free AAQ dye, **b** DTAD, and **c** the DTAD-Au NRs

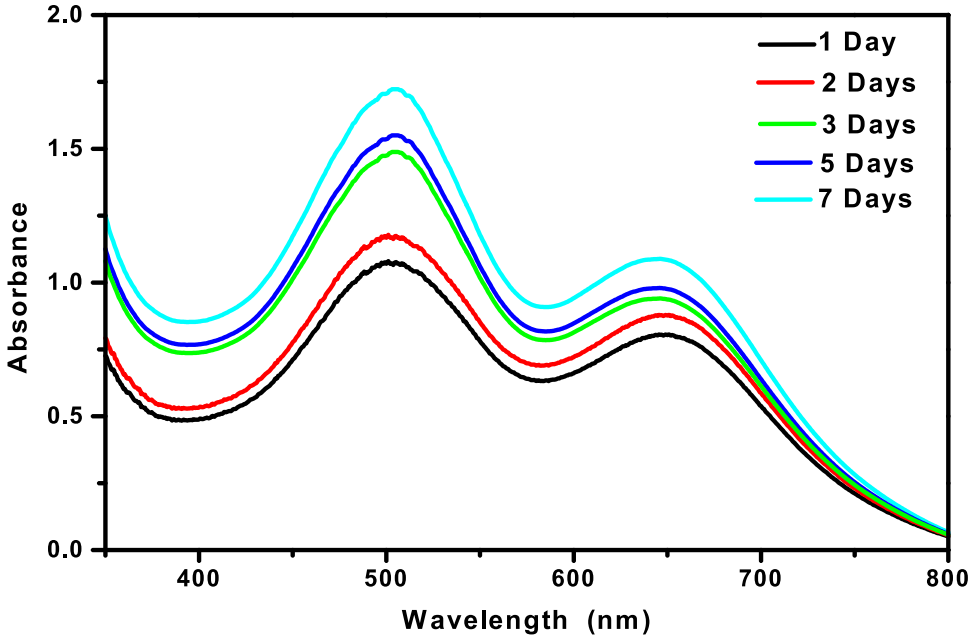

Fig. 7 Absorption spectra of DTAD-Au NRs recorded at different days

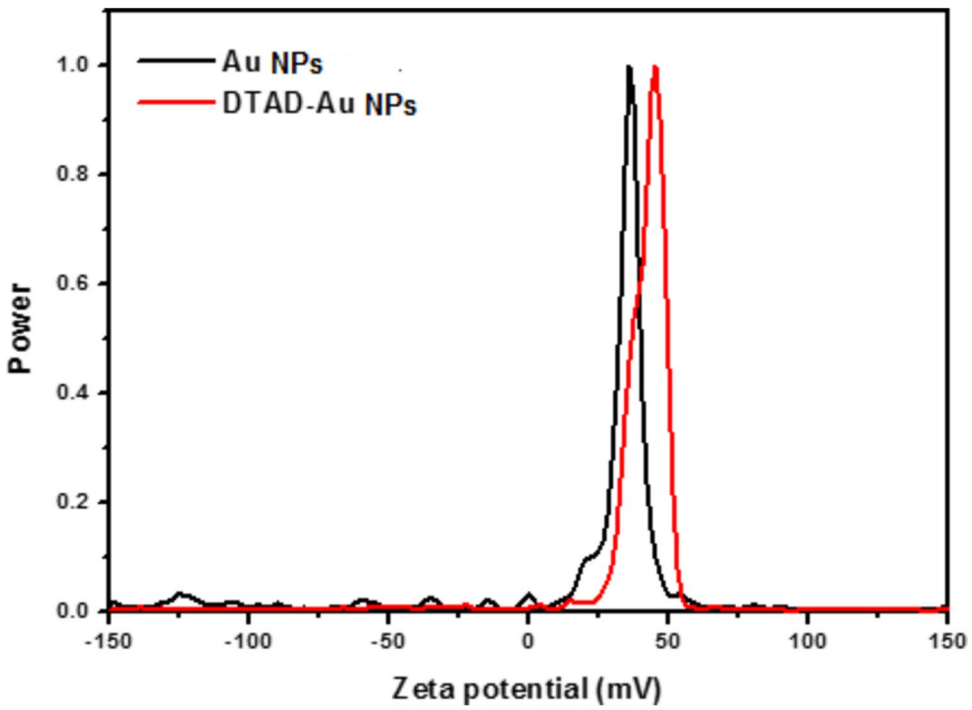

Fig. 8 The Zeta potentials of Au NRs and DTAD-Au NRs

Sensing response of DTAD-Au NRs chemosensor to metal ions

Using the steady-state absorption technique, the sensitivity of the DTAD-Au NRs chemosensor to various metal ions, including Mg^{2+}, K^{+}, Ca^{2+}, Mn^{2+}, Fe^{3+}, Co^{2+}, Ni^{2+}, Cu^{2+}, Zn^{2+}, Cd^{2+}, and Pb^{2+}, was examined. The absorption spectra of DTAD-Au NRs after the addition of various metal ions are shown in Fig. 9. The findings demonstrate that DTAD-Au NRs still exhibit high sensitivity to the studied metal ions.

Figure 10 displays the chemosensor's absorption spectra in the absence and presence of various concentrations of the used metal ions ($0.0–1.6\times10^{-3}$ M). It is evident that when Mg^{2+}, K^{+}, Ca^{2+}, and Cu^{2+} ions are added to the DTAD-Au NRs solution, the absorption spectra gradually decrease as the concentrations of the aforementioned metal ions increase. However, upon adding Co^{2+} salt solutions,

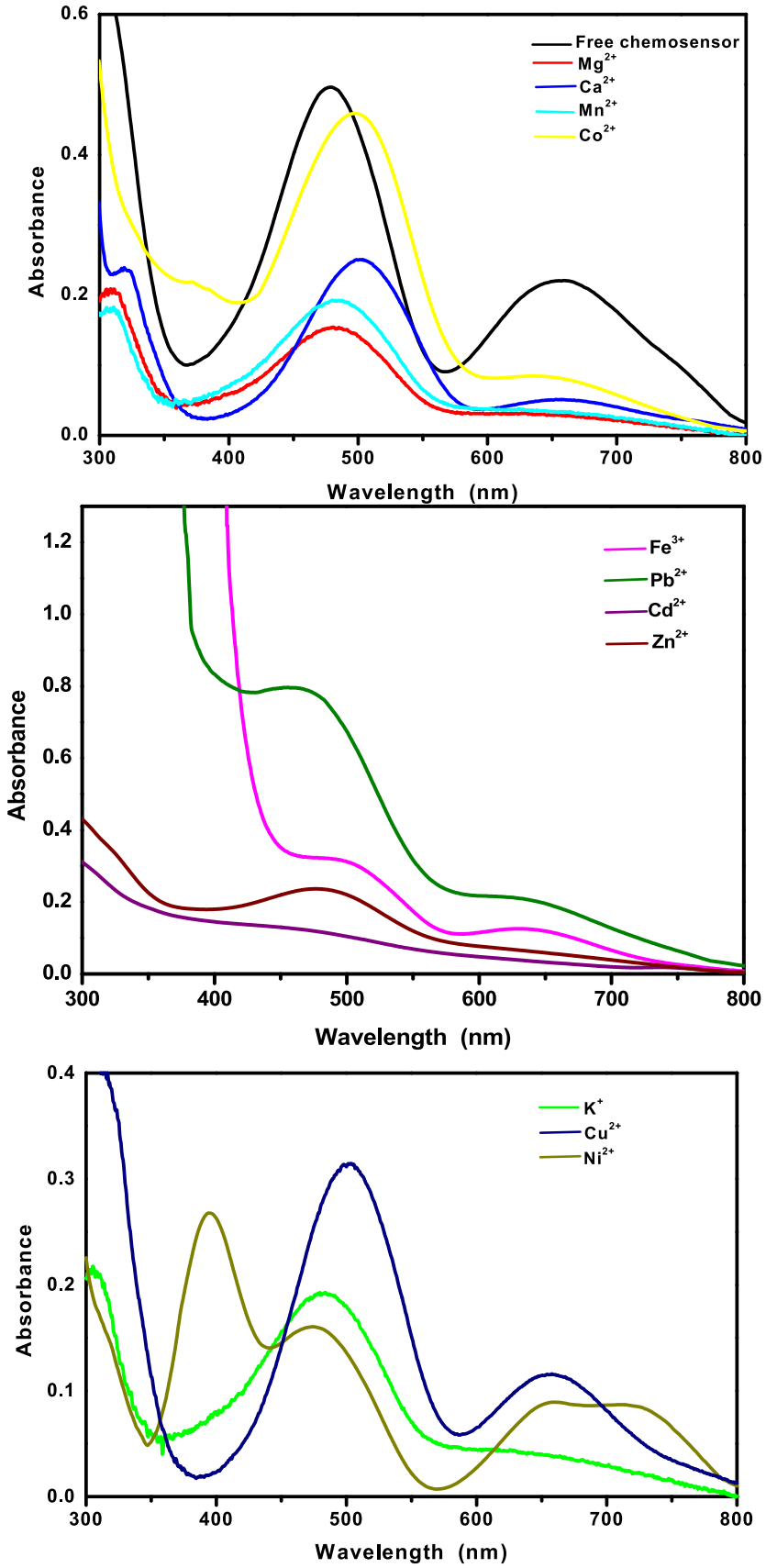

Fig. 9 The absorption spectra of DTAD-Au NRs chemosensor in the presence of different metal ions

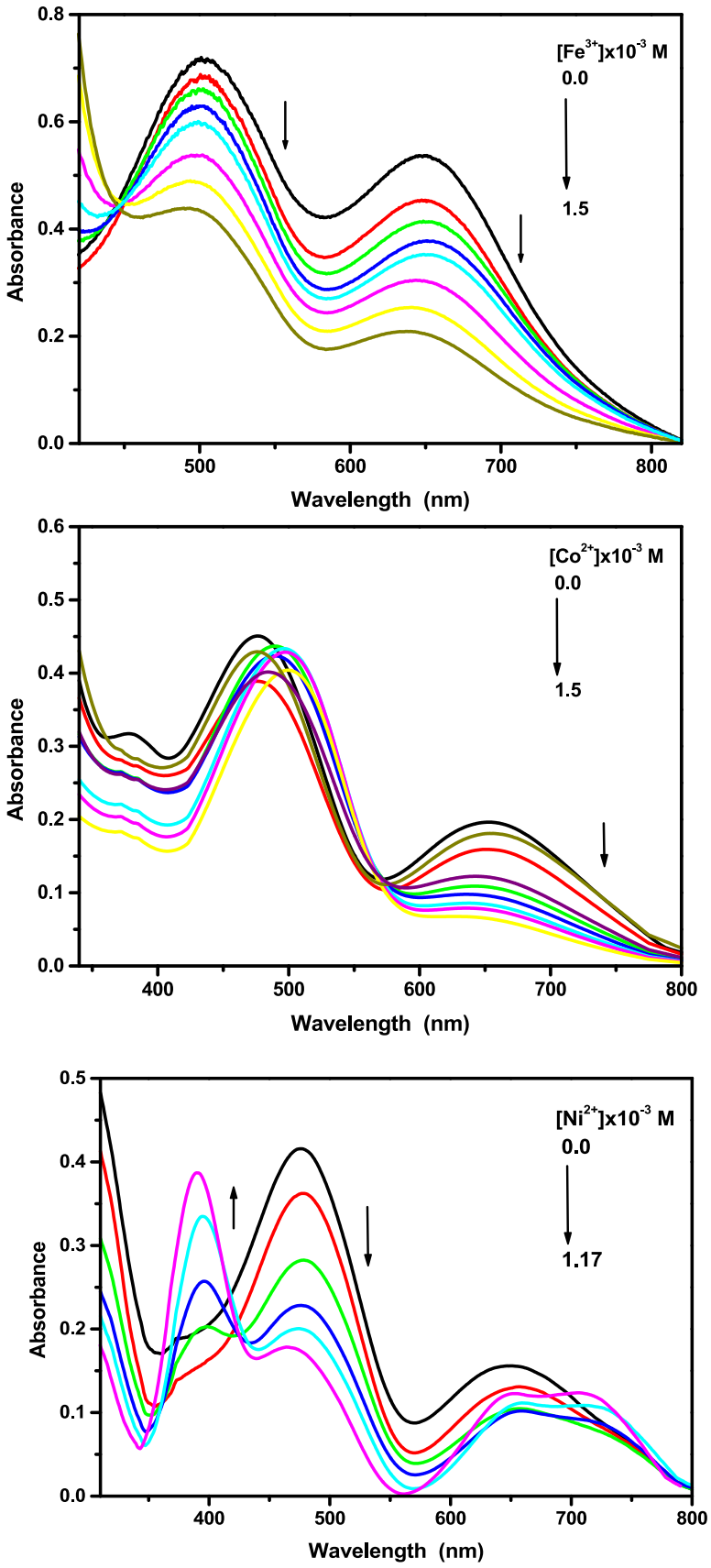

Fig. 10 The absorption spectra of DTAD-Au NRs chemosensor in the absence and presence of different concentrations of the mentioned metal ions

the DTAD-Au NRs chemosensor's absorption maximum at 495 and 650 nm decreased and a new band with the creation of an isosbestic point at 440 nm was generated at 502 nm.

After addition of Fe^{3+} ions to DTAD-Au NRs solution, the absorption maximum was decreased with formation of an isosbestic point at 440 nm. A new band around 395 nm was also developed when Ni^{2+} salt solutions were added to the chemosensor, and the absorption band at 650 nm was shifted to a longer wavelength with the formation of an isosbestic point at 423 nm at higher concentrations of Ni^{2+} ions (6.2×10^{-4}–1.17×10^{-3} M). The absorption band of DTAD-Au NRs gradually increased with the development of a shoulder around 469 nm after the addition of Pb^{2+} ions, whereas with Cd^{2+} ions, the absorption band decreased with the formation of a shoulder at greater concentrations. In case of adding Zn^{2+} ions, the absorption spectra decrease gradually with formation of two isosbestic points at 433 and 576 nm, at higher concentrations.

The impact of adding various metal ion concentrations on the emission spectra of the chemosensor is depicted in Fig. 11. When adding various metal ion concentrations, the free chemosensor DTAD-Au NRs (located at 590 nm) typically experience a steady increase in fluorescence intensity without a discernible shift in the emission maxima. Since the intensity of the fluorescence spectrum of the chemosensor molecules has increased, the spectral alterations prove that the free chemosensor and the metal ions have complexed. Additionally, the spectrum behavior suggests that the studied chemical may be employed as 'off–on' switchable chemosensor for metal ion detection.

The binding constants based on the fluorescence measurements were calculated using modified Benesi–Hildebrand equation [37];

$$1/\left(F-F_o\right)=1/K_b\left(F_{\max}-F_o\right)\left[\mathrm{M^{n+}}\right]+1/\left(F_{\max}-F_o\right)$$

The K_b values derived from the slopes of the straight line of $1/(F-F_o)$ vs. $[M^{n+}]$, Fig. 12, are summarized in Table 1. A cursory glance at the reported data reveals found that K_b values follow the order; $Cd^{2+} > Fe^{3+} > Zn^{2+} > Mg^{2+} > Cu^{2+} > Co^{2+} > Ni^{2+} > Mn^{2+} > Ca^{2+} > K^{+} > Pb^{2+}$. This order confirms that DTAD-Au NRs have strongest binding tendency toward Cd^{2+} ions compared to the other metal ions, which was attributed to strong chelation of Cd^{2+}ion with the free chemosensor. Additionally, it is found that, in comparison with other ions, the DTAD-Au NRs chemosensor has a high level of specificity in recognizing Cd^{2+} ions.

The potential interferences by the co-existing metal ions, Mg^{2+}, K^{+}, Ca^{2+}, Mn^{2+}, Fe^{3+}, Co^{2+}, Ni^{2+}, Cu^{2+}, Zn^{2+}, and Pb^{2+} in the presence of Cd^{2+} ions, were investigated in order to assess the practical applicability of DTAD-Au NRs as a selective chemosensor. The fluorescence changes of the chemosensor were measured using 1.3×10^{-3} M Cd^{2+}, in the presence of the following interfering metal ions: Mg^{2+}, K^{+}, Ca^{2+}, Mn^{2+}, Fe^{3+}, Co^{2+}, Ni^{2+}, Cu^{2+}, Zn^{2+}, and Pb^{2+}. The emission intensities of the examined interfering metal ions

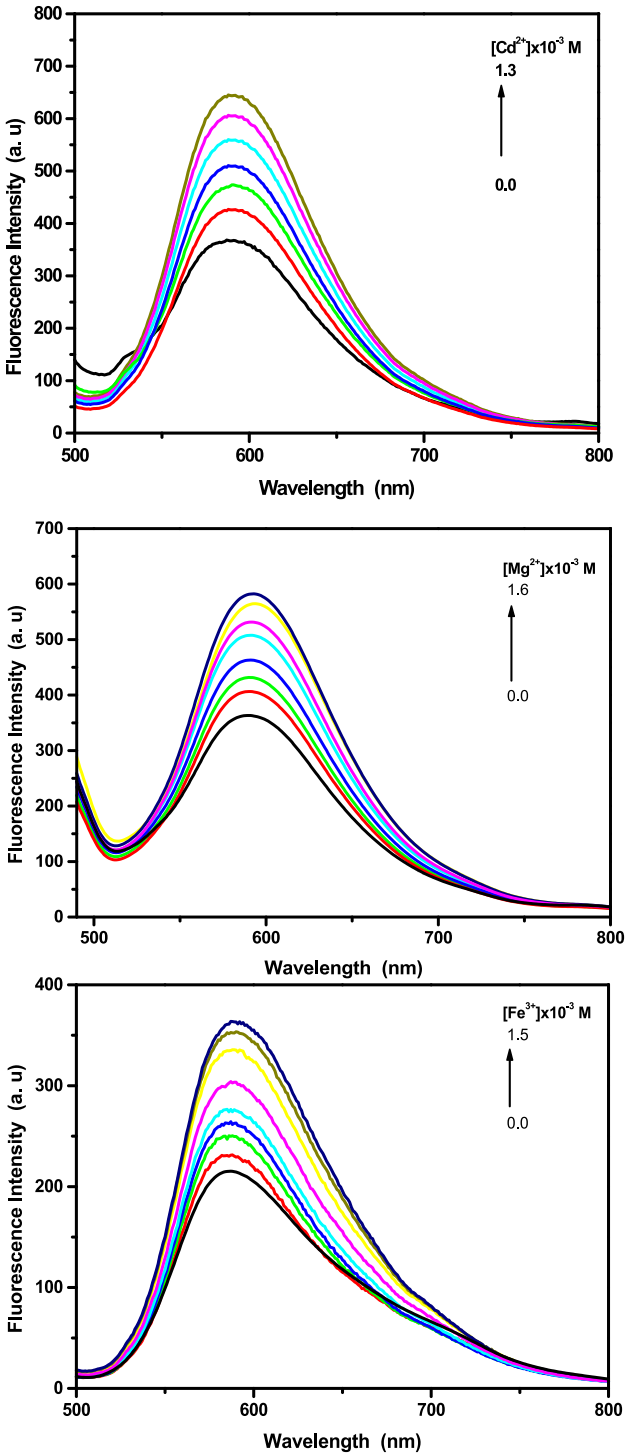

Fig. 11 The fluorescence spectra of DTAD-Au NRs chemosensor in the absence and presence of different concentrations of the mentioned metal ions

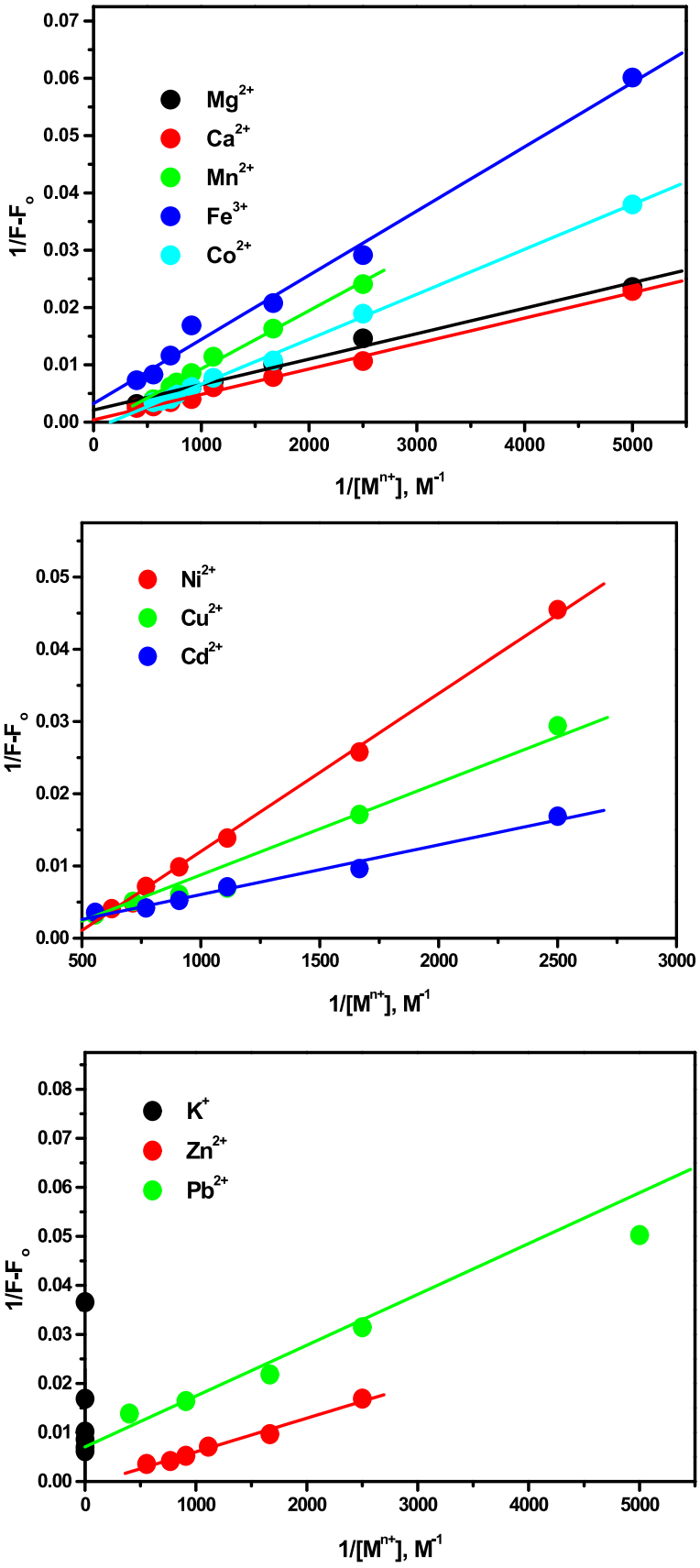

Fig. 12 Benesi–Hildebrand plots for the complexation between DTAD-Au NRs chemosensor and the mentioned metal ions

Table 1 Spectroscopic parameters and the excited state binding constant for DTAD-Au NRs chemosensor with the used metal ions

Metal ion	λ^{a}_{max} nm	λ^{f}_{max} nm	$K_b \times 10^3$ (M^{-1})
Free DTAD-Au NRs	478, 660	589	–
Mg^{+}	481, 642	595	1.66
K^{+}	486,657	592	0.55
Ca^{2+}	504, 657	593	0.56
Mn^{2+}	481, 662	592	0.64
Fe^{3+}	500, 644	594	2.05
Co^{2+}	499, 664	593	1.11
Ni^{2+}	391, 482, 674	589	0.73
Cu^{2+}	502, 659	592	1.36
Cd^{2+}	468, 669	591	3.16
Zn^{2+}	482, 648	592	1.87
Pb^{2+}	468, 633	592	0.53

did not significantly vary during the detection of Cd^{2+} ion, as seen in Fig. 13. The same concentration of the other metal ions does not, in fact, have any impact on the DTAD-Au NRs' fluorescence enhancement response for Cd^{2+}. These findings demonstrate the potential of using DTAD-Au NRs for real-sample applications including the selective detection of Cd^{2+} ions.

Bio-imaging studies

In the presence of Cd^{2+} ions, the synthesized substances DTAD, Au NRs, and DTAD-Au NRs were examined for cell staining and imaging using a fluorescent microscope, as shown in Fig. 14. The current study's findings show that both DTAD and Au NRs are less effective staining agents for the nucleus as well as some focused cytoplasmic regions that might be mitochondrial DNA. For DTAD-Au NRs and DTAD-Au NRs/Cd^{2+}, however, only the nuclei were stained, resulting in a strong green fluorescence and bright field from the intercellular region. This confirms that both DTAD-Au NRs and DTAD-Au NRs/Cd^{2+} could effectively stain the nuclei as well as some focal cytoplasmic areas that were thought to be mitochondrial DNA.

It has been hypothesized that DTAD-Au NRs in the presence of Cd^{2+} ions are more effective and may even be similar to DAPI (4,6-diamidino-2-phenylindole), which has been used successfully for decades to stain DNA [38]. According to the results of the fluorescence microscopic investigation, the DTAD-Au NRs chemosensor has good cell permeability, is capable of binding with Cd^{2+} ions in living cells, and has high fluorescence imaging. The acquired results agree well with the aforementioned emission studies. As a result, it can be suggested to use this chemosensor as a probe for Cd^{2+} ions in biological systems.

In vitro studies

Effect of Au NRs and DTAD-Au NRs on cancer cell proliferation

Gold nanorods are now recognized as a potent nanoagent for the diagnosis and treatment of cancer. Three cancer cell lines were subjected to the MTT assay to evaluate the impact of AuNPs and DTAD-Au NRs concentrations on cell viability as shown in Fig. 15. As the concentrations of AuNPs and DTAD-Au NRs increase, the percentage of HepG-2, MCF-7, and Caco-2 cells death steadily increase, where Au NRs had IC_{50} values of 1.971 ± 1.28, 3.752 ± 2.12, and 27.33 ± 2.86, µg/mL for the HepG-2, MCF-7, and Caco-2 cell lines, respectively. Additionally, DTAD-Au NRs had IC_{50} values of 40.95 ± 2.56, 51.72 ± 3.53, and 79.38 ± 3.5 µg/mL for the HepG-2, MCF-7, and Caco-2 cell lines, respectively. Our results demonstrated that Au NRs significantly inhibited the growth of all cancer cells than DTAD-Au

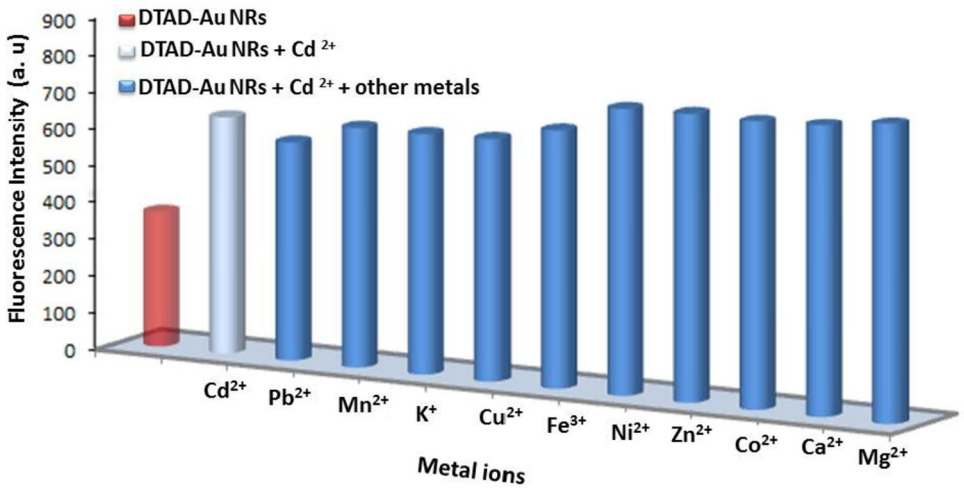

Fig. 13 Selectivity of DTAD-Au NRs-Cd^{2+} over the different metal ions

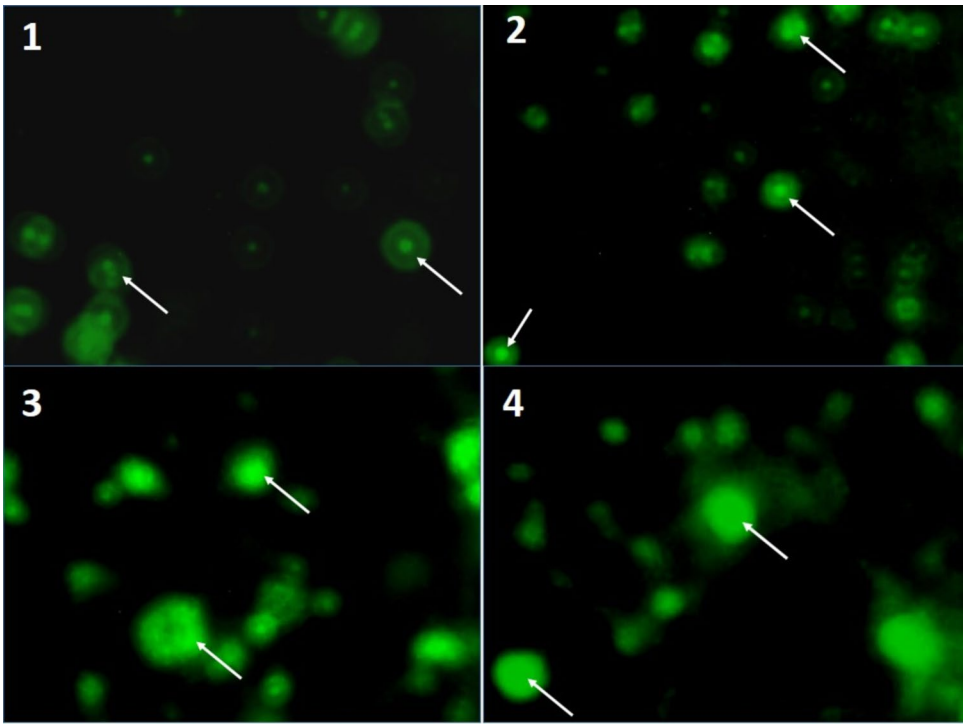

Fig. 14 **1** Fluorescent photomicrograph of free AAQ dye showing weak nuclear and cytoplasmic staining (arrows), while **2** fluorescent photomicrograph of Au NRs showing moderate nuclear and cytoplasmic staining (arrows) in different mononuclear cells, and **3**, **4** fluorescent photomicrographs of DTAD-Au NRs and DTAD-Au NRs/Cd^{2+}, respectively, showing strong nuclear and cytoplasmic staining in different mononuclear cells (arrows)

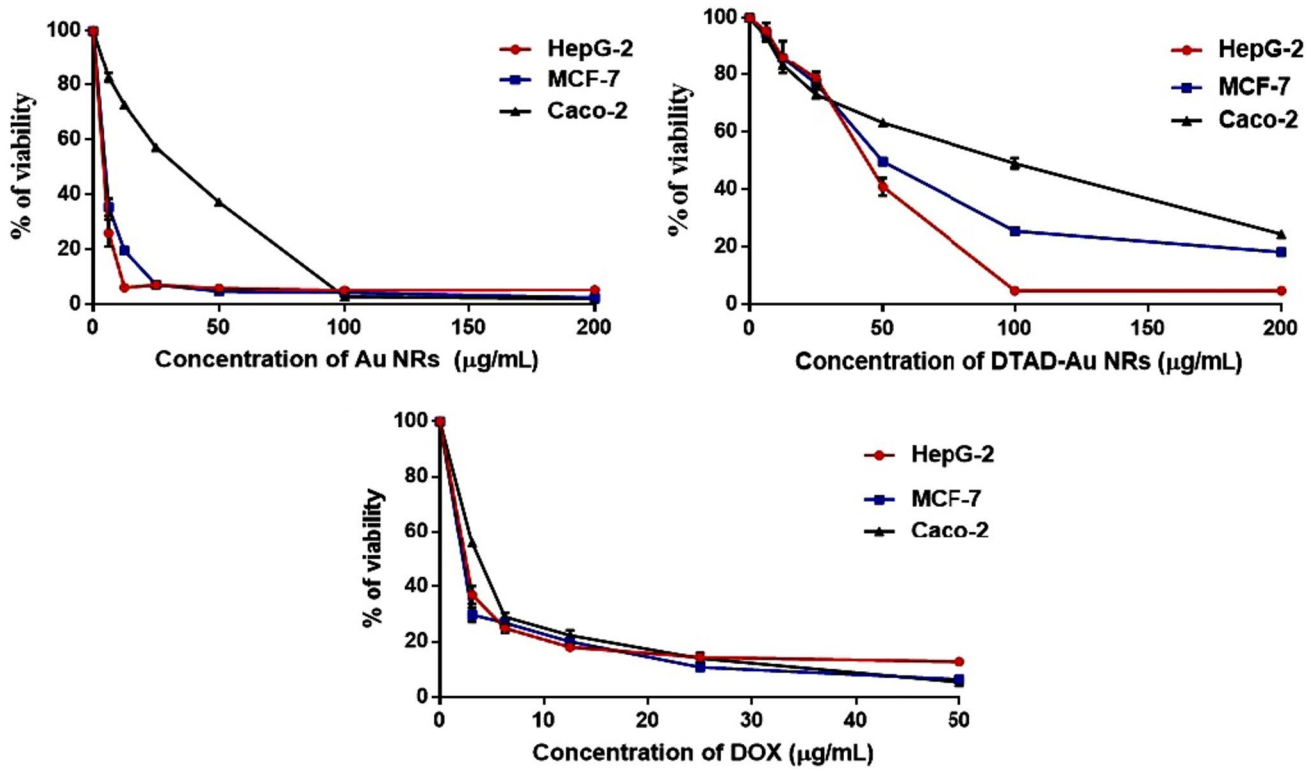

Fig. 15 Anticancer effects of Au NRs, DTAD-Au NRs, and doxorubicin on HepG-2, MCF-7, and Caco-2 cell lines. Cells were treated for 48 h, and results were expressed as mean ± SE. The experiment done in triplicate

NRs with best antiproliferative effect on HepG-2 hepatocellular carcinoma compared to DOX, the standard chemotherapeutic drug on HepG-2, MCF-7, and Caco-2 cell lines ($IC_{50} = 1.036 \pm 1.02$, 0.852 ± 0.9, and 3.430 ± 1.7 µg/mL), respectively. Thus, HepG-2 cancer cells were chosen for further analysis. According to the previous studies our results were in line with Muthukumar et al. [39], who study the effect of gold nanoparticles and their enhanced synergistic antitumor activity using HepG2 and MCF7 cells. Also, Nandhini et al. [40], Mousavi-Kouhi et al. [41], and Kong et al. [42] elucidated the effect of Au NRs on HepG2, MCF-7, and Caco-2 cells. Moreover, Shakerimanesh et al. [43, 44] observed the effectiveness of the Au NPs on the mouse breast cancer cells with lesser toxicity.

Cellular morphology changes

Apoptosis is essential for controlling the development and spread of cancer cells [45]. Morphological changes are the first line of evidence for a drug's ability to induce apoptosis. As well, gold nanorods alter cancer cell morphology, decrease in cell quantity, and increase in amount of cell debris. Here, HepG-2 hepatocellular carcinoma treated with Au NRs showed visible morphological signs of apoptosis in its IC_{50} concentration including cytoplasmic condensation, and cell detachment than IC_{50} of DTAD-Au NRs that showed moderate apoptotic effect compared with the untreated cells that has normal morphological appearance, spindle, and confluent as shown in Fig. 16.

Annexin V flow cytometry apoptotic evaluations

Specific morphological characteristics, including as loss of plasma membrane asymmetry, plasma membrane blebbing, DNA inter-nucleosomal cleavage, and condensation of the cytoplasm, were defined the apoptotic process. Therefore, to distinguish between early and late apoptotic cells, Annexin V labeling is frequently combined with a crucial dye, such as propidium iodide (PI), whereas dead cell membranes allow PI through, while healthy cell membranes keep out PI [46]. The results showed that the incubation of HepG-2 cells with the IC_{50} of Au NRs for 48 h observed a good apoptotic effect as 13.26% of cells being in early apoptosis, 1.65% of cells being in late apoptosis, and 10.23% of cells were necrotic compared with the untreated control cells. While the incubation of cells with the IC_{50} of DTAD-Au NRs shows moderate apoptotic effect as it examined only 4.21% of cells being in early apoptosis, 0.25% of cells being in late apoptosis and 6.57% of cells were necrotic compared with the untreated control cells (Fig. 17). There are several reports studied the apoptotic effect of gold nanorod on the proliferation of different types of cancer cells. For instance, Chen et al. [47] showed the apoptotic effect of gold nanorods conjugated with doxorubicin using annexin V in vivo. Furthermore, Qin et al. [48] studied the apoptotic effect of gold nanorods in vivo and in vitro using annexin V. From the previous view, we elucidated that gold nanorod inhibits the proliferation of cancer cells by inducing apoptosis.

Conclusion

In summary, a novel gold nanorods-based colorimetric chemosensor has been fabricated using functionalized gold nanorods with (9,10-dioxo-9,10-dihydro-anthracen-1-yl)-dithiocarbamic acid, DTAD for simple, rapid, and simultaneous detection of toxic metal ions. The optical sensing response toward Mg^{2+}, K^{+}, Ca^{2+}, Mn^{2+}, Fe^{3+}, Co^{2+}, Ni^{2+}, Cu^{2+}, Zn^{2+}, Cd^{2+}, and Pb^{2+} ions was investigated. The results indicate that the investigated chemosensor can be used efficiently to identify all of the investigated metal ions, with high sensitivity and selectivity to Cd^{2+} ions, compared to the others. Furthermore, the biological chemosensing applications of the novel investigated chemosensor to Cd^{2+} ions was demonstrated for fluorescence imaging experiments in living cells. The fluorescence images grew brighter with Cd^{2+}, compared to that recorded with the free chemosensor, supporting that compound is an effective fluorescent sensor

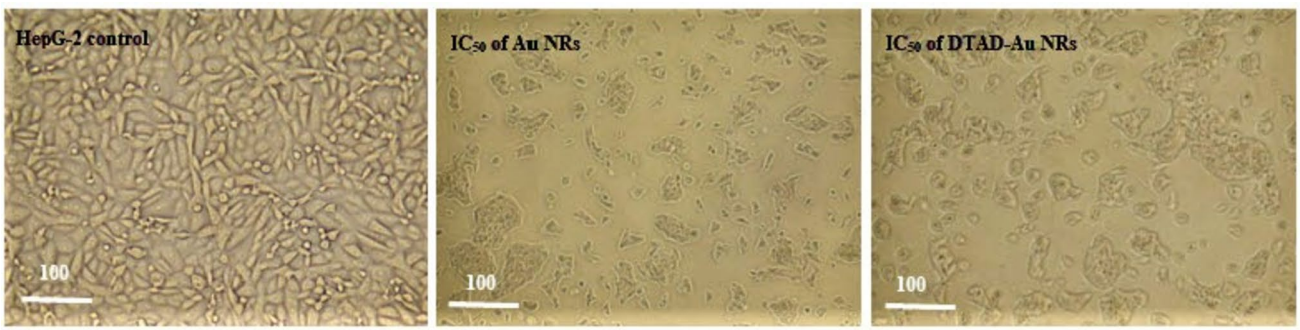

Fig. 16 Morphological alterations of Au NRs and DTAD-Au NRs on HepG-2 cancer cells after treated for 48 h

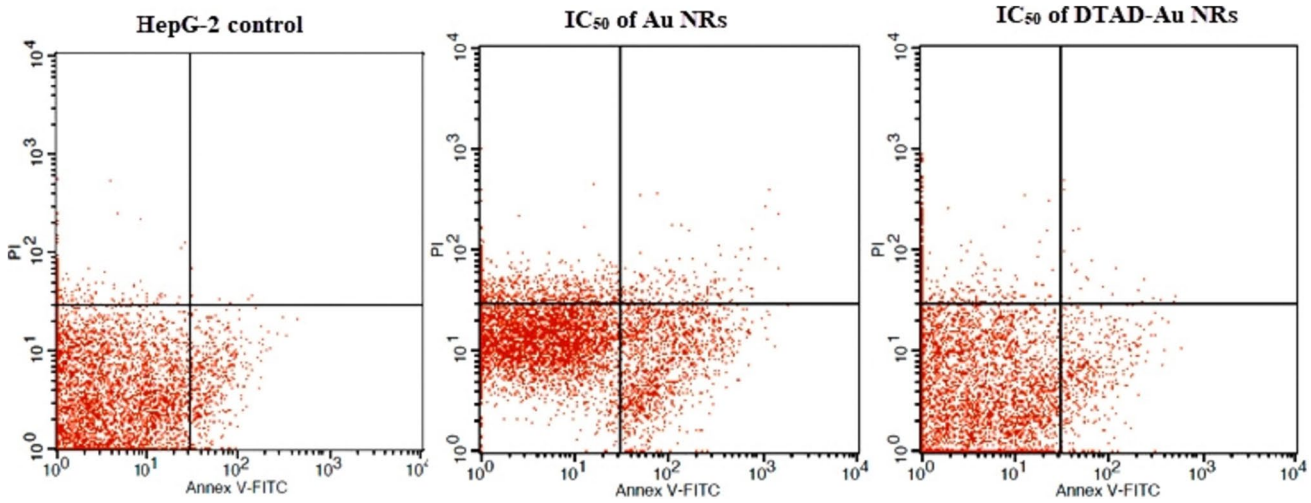

Fig. 17 Apoptotic features of Au NRs and DTAD-Au NRs on HepG-2 cancer cells after treated for 48 h using Annexin V flow cytometry

for Cd^{2+} metal ion. Moreover, this study elucidated that Au NRs have a potent inhibitory effect on the proliferation of HepG-2 hepatocellular carcinoma, while DTAD-Au NRs have a moderate effect. The apoptotic effect of Au NRs and DTAD-Au NRs was confirmed by the loss of plasma membrane asymmetry which leads to increasing the apoptotic cells percentage that detected using Annexin V flow cytometric analysis. As a result of these findings, gold nanorods may one day be employed to treat human liver cancer.

Acknowledgements The authors are grateful to the Scientific Research Fund at Tanta University, Egypt, for funding this work through research project code TU:02-19-03. Also, we are grateful to Dr/Heba Hassan, MD, Department of Histology, Faculty of Medicine, Tanta University, for her helping in the biological studies.

Funding Open access funding provided by The Science, Technology & Innovation Funding Authority (STDF) in cooperation with The Egyptian Knowledge Bank (EKB).

Declarations

Conflict of interest The authors declare that they have no known competing financial interests or personal relationships that could have appeared to influence the work reported in this paper.

References

1. Y. Fu, R.A. Ganeev, P.S. Krishnendu, C. Zhou, K.S. Rao, C. Guo, Size-dependent off-resonant nonlinear optical properties of gold nanorods and demonstration of efficient optical limiting. Opt. Mater. Express **9**, 976–991 (2019). https://doi.org/10.1364/OME.9.000976
2. S.C. Mehendale, S.R. Mishra, K.S. Bindra, M. Laghate, T.S. Dhami, K.S. Rustagi, Nonlinear refraction in aqueous colloidal gold. Opt. Commun. **133**, 273–276 (1997). https://doi.org/10.1016/S0030-4018(96)00431-2
3. X. Huang, S. Neretina, M.A. El-Sayed, Gold nanorods: from synthesis and properties to biological and biomedical applications. Adv. Mater. **21**, 4880–4910 (2009). https://doi.org/10.1002/adma.200802789
4. C.J. Murphy, T.K. Sau, A.M. Gole, C.J. Orendorff, J. Gao, L.S. Gou, E. Hunyadi, T. Li, J. Phys. Chem. B **109**, 13857–13870 (2005). https://doi.org/10.1021/jp0516846
5. J. Kumar, K.G. Thomas, Surface-enhanced raman spectroscopy: investigations at the nanorod edges and dimer junctions. J. Phys. Chem. Lett. **2**, 610–615 (2011). https://doi.org/10.1021/jz2000613
6. D. Solis, W.-S. Chang, B.P. Khanal, K. Bao, P. Nordlander, E.R. Zubarev, S. Link, Bleach-imaged plasmon propagation (BIIPP) in single gold nanowires. Nano Lett. **10**, 3482–3485 (2010). https://doi.org/10.1021/nl1016128
7. B. Wild, L. Cao, Y. Sun, B.P. Khanal, E.R. Zubarev, S.K. Gray, N.F. Scherer, M. Pelton, Propagation lengths and group velocities of plasmons in chemically synthesized gold and silver nanowires. ACS Nano **6**, 472–482 (2012). https://doi.org/10.1021/nn203802e
8. L.C. Kennedy, L.R. Bickford, N.A. Lewinski, A.J. Coughlin, Y. Hu, E.S. Day, J.L. West, R.A. Drezek, A new era for cancer treatment: Gold-nanoparticle-mediated thermal therapies. Small **7**, 169–183 (2011). https://doi.org/10.1002/smll.201000134
9. M. Akif, A.R. Khan, K. Sok, Textile effluents and their contribution towards aquatic pollution in the Kabul river (Pakistan). J. Chem. Soc. Pak. **24**, 106–111 (2002)
10. G. Rajaei, B. Mansouri, H. Jahantigh, A.H. Hamidian, Metal concentrations in the water of Chah nimeh reservoirs in Zabol, Iran. Bull. Environ. ContamToxicol. **89**, 495–500 (2012). https://doi.org/10.1007/s00128-012-0738-0
11. K.G. Ravindra, K.S. Sanjay, M. Suresh, C.C. Mahesh, CHAPTER 1: contamination of heavy metals in aquatic media: transport,

toxicity and technologies for remediation, *in* Heavy Metals in Water: Presence, Removal and Safety. RSC Advances (2014) 1–24. https://doi.org/10.1039/9781782620174-00001
12. B.C. Janegitz, L.H. Marcolino-Junior, S.P. Campana-Filho, R.C. Faria, O. Fatibello-Filho, Anodic stripping voltammetric determination of copper (II) using a functionalized carbon nanotubes paste electrode modified with crosslinked chitosan. Sens. Actuators B **142**, 260–266 (2009). https://doi.org/10.1016/j.snb.2009.08.033
13. M.H. Mashhadizadeh, M. Pesteh, M. Talakesh, I. Sheikhshoaie, M.M. Ardakani, M.A. Karimi, Solid phase extraction of copper (II) by sorption on octadecyl silica membrane disk modified with a new Schiff base and determination with atomic absorption spectrometry. Spectrochim. Acta B **63**, 885–888 (2008). https://doi.org/10.1016/j.sab.2008.03.018
14. M.L. Desai, H. Basu, S. Saha, R.K. Singhal, S.K. Kailasa, Fluorescence enhancement of bovine serum albumin gold nanoclusters from La^{3+} ion: detection of four divalent metal ions (Hg^{2+}, Cu^{2+}, Pb^{2+} and Cd^{2+}). J. Mol. Liquids. **336**, 116239 (2021). https://doi.org/10.1016/j.molliq.2021.116239
15. J.R. Bhamore, A.R. Gul, S.K. Kailasa, K.-W. Kim, J.S. Lee, H. Park, T.J. Park, Functionalization of gold nanoparticles using guanidine thiocyanate for sensitive and selective visual detection of Cd^{2+}. Sens. Actuators B Chem. **334**, 129685 (2021). https://doi.org/10.1016/j.snb.2021.129685
16. M.N. El-Nahass, D. Abd El-Aziz, T.A. Fayed, Selective "on–off–on" switchable chemosensor for metal ions detection and its complexes. Sens. Actu. B Chem. **205**, 377–390 (2014). https://doi.org/10.1016/j.snb.2014.08.067
17. M.N. El-Nahass, T.A. Fayed, Chemosensing hybrid materials: chalcones-functionalized cage-like mesoporous SBA-16 material for highly selective detection of toxic metal ions. Appl. Organomet. Chem. **31**, 1–13 (2017). https://doi.org/10.1002/aoc.3751
18. M.N. El-Nahass, T.A. Fayed, M.H. Shaaban, F.M. Hassan, Chalcone isothiocyanate-mesoporous silicates: selective anchoring and toxic metal ions detection. Sens. Actu. B Chem. **210**, 56–68 (2015). https://doi.org/10.1016/j.snb.2014.12.079
19. T.A. Fayed, M.A. El-morsi, M.N. El-Nahass, Intramolecular charge transfer emission of a new ketocyanine dye: effects of hydrogen bonding and electrolyte. J. Photochem. Photobiol. A: Chem. **224**, 38–45 (2011). https://doi.org/10.1016/j.jphotochem.2011.09.004
20. M. Gaber, T.A. Fayed, M.N. El-Nahass, H.A. Diab, M.M. El-Gamil, Synthesis spectroscopic characterization and biological evaluation of a novel chemosensor with different metal ions. Appl. Organometal. Chem. (2019). https://doi.org/10.1002/aoc.5133
21. M. Sabela, S.B. Baekeland, J.M. Janot, K. Bisetty, A review of gold and silver nanoparticle-based colorimetric sensing assays. Adv. Eng. Mater. **19**, 1700270 (2017). https://doi.org/10.1002/adem.201700270
22. X. Huang, P.K. Jain, I.H. El-Sayed, M.A. El-Sayed, Determination of the minimum temperature required for selective photothermal destruction of cancer cells with the use of immunotargeted gold nanoparticles. Photochem. Photobiol. **82**, 412–417 (2006). https://doi.org/10.1562/2005-12-14-RA-754
23. S. Rajeshkumar, Anticancer activity of eco-friendly gold nanoparticles against lung and liver cancer cells. J. Genet. Eng. Biotechnol. **14**, 195–202 (2016). https://doi.org/10.1016/j.jgeb.2016.05.007
24. S.K. Kailasa, S. Borse, J.R. Koduru, Z.V.P. Murthy, Biomolecules as promising ligands in the synthesis of metal nanoclusters: sensing, bioimaging and catalytic applications. Trends Environ. Anal. Chem. **32**, e00140 (2021). https://doi.org/10.1016/j.teac.2021.e00140
25. V.N. Mehta, J.V. Rohitm, S.K. Kailasa, Functionalization of silver nanoparticles with 5-sulfoanthranilic acid dithiocarbamate for selective colorimetric detection of Mn^{2+} and Cd^{2+} ions. New J. Chem. **40**, 4566–4574 (2016). https://doi.org/10.1039/C5NJ03454J
26. J.F. Ivan, E.K. Marjorie, D.S. Phillip, Z. Heddy, Isolation of whole mononuclear cells from peripheral blood and cord blood. Current Protocols **85**, 7.1.1-7.1.8 (2009). https://doi.org/10.1002/0471142735.im0701s85
27. A.A. Noser, A.H. Abdelmonsef, M.M. Salem, Design, synthesis and molecular docking of novel substituted azepines as inhibitors of PI3K/Akt/TSC2/mTOR signaling pathway in colorectal carcinoma. Bioorg. Chem. (2022). https://doi.org/10.1016/j.bioorg.2022.106299
28. X. Wu, Z. Huang, J. Liu, Y. Chen, H. Huang, Y. He, D. Li, L. Zhang, Z. Du, K. Zhang, S. Goodin, X. Zheng, Effects and mechanism of inhibition of naringin in combination with atorvastatin on prostate cancer cells in vitro and in vivo. Phytochem. Lett. **32**, 168–176 (2019). https://doi.org/10.1016/j.phytol.2019.06.008
29. S. Kim, J.H. Lee, G. Sethi, C. Kim, S.H. Baek, D. Nam, W. Chung, S. Kim, B.S. Shim, K.S. Ahn, Bergamottin, a natural furanocoumarin obtained from grapefruit juice induces chemosensitization and apoptosis through the inhibition of STAT3 signaling pathway in tumor cells. Cancer lett. **354**, 153–163 (2014). https://doi.org/10.1016/j.canlet.2014.08.002
30. M.I. Gamal, N.M. Fahmy, F. Wu, M.M. Salem, O.M. Khattab, H.R. El-Seedi, M. Korinek, T. Hwang, A.K. Osman, M. El-Shazly, S. Fayez, Comparative LC–LTQ–MS–MS analysis of the leaf extracts of lantana camara and lantana montevidensis growing in Egypt with insights into their antioxidant, anti-inflammatory, and cytotoxic activities. Plants. **11**, 1699 (2022). https://doi.org/10.3390/plants11131699
31. T. Placido, R. Comparelli, F. Giannici, P.D. Cozzoli, G. Capitani, M. Striccoli, A. Agostiano, M.L. Curri, Photochemical synthesis of water-soluble gold nanorods: the role of silver in assisting anisotropic growth. Chem. Mater. **21**, 4192–4202 (2009). https://doi.org/10.1021/cm900721r
32. T.K. Sau, C.J.J. Murphy, Room temperature, high-yield synthesis of multiple shapes of gold nanoparticles in aqueous solution. Am. Chem. Soc. **126**, 8648–8649 (2004). https://doi.org/10.1021/ja047846d
33. M.Z. Liu, P. Guyot-Sionnest, Mechanism of silver(I)-assisted growth of gold nanorods and bipyramids. J. Phys. Chem. B **109**, 22192–22200 (2005). https://doi.org/10.1021/jp054808n
34. K. Nishioka, Y. Niidome, S. Yamada, Photochemical reactions of ketones to synthesize gold nanorods. Langmuir **23**, 10353–10356 (2007). https://doi.org/10.1021/la7015534
35. H.M. Chen, C.F. Hsin, R.-S. Liu, J.-F. Lee, L.-Y. Jang, Synthesis and characterization of multi-pod-shaped gold/silver nanostructures. J. Phys. Chem. C **111**, 5909–5914 (2007). https://doi.org/10.1021/jp070232l
36. Z.-C. Xu, C.-M. Shen, C.-W. Xiao, T.-Z. Yang, H.-R. Zhang, J.-Q. Li, H.-L. Li, H.-J. Gao, Wet chemical synthesis of gold nanoparticles using silver seeds: a shape control from nanorods to hollow spherical nanoparticles. Nanotechnology **18**, 115608 (2007). https://doi.org/10.1088/0957-4484/18/11/115608
37. L.M. Benesi, H.J. Hildebrand, A spectrophotometric investigation of the interaction of iodine with aromatic hydrocarbons. J. Am. Chem. Soc. **71**, 2703–2707 (1949). https://doi.org/10.1021/ja01176a030
38. J. Kapuscinski, DAPI: a DNA-specific fluorescent probe. J. Biotech, Histochem. **70**, 220–233 (1995). https://doi.org/10.3109/10520299509108199
39. T. Muthukumar, B. Sambandam, A. Aravinthan, T.P. Sastry, J.H. Kim, Green synthesis of gold nanoparticles and their enhanced synergistic antitumor activity using HepG2 and MCF7 cells and its antibacterial effects. Process Biochem. **51**, 384–391 (2016). https://doi.org/10.1016/j.procbio.2015.12.017

40. J.T. Nandhini, D. Ezhilarasan, S. Rajeshkumar, An ecofriendly synthesized gold nanoparticles induces cytotoxicity via apoptosis in HepG2 cells. Environ. Toxicol. **36**, 24–32 (2021). https://doi.org/10.1002/tox.23007
41. S.M. Mousavi-Kouhi, A. Beyk-Khormizi, V. Mohammadzadeh, M. Ashna, A. Es-haghi, M. Mashreghi, V. Hashemzadeh, H. Mozafarri, M. Nadaf, M.E. Taghavizadeh Yazdi, Biological synthesis and characterization of gold nanoparticles using Verbascum speciosum Schrad. and cytotoxicity properties toward HepG2 cancer cell line. Res. Chem. Intermed. **48**, 167–178 (2022). https://doi.org/10.1007/s11164-021-04600-w
42. X. Kong, Y. Sun, Q. Zhang, S. Li, Y. Jia, R. Li, Y. Liu, Z. Xie, Specific tumor cell detection by a metabolically targeted aggregation-induced emission-based gold nanoprobe. ACS Omega **7**, 18073–18084 (2022). https://doi.org/10.1021/acsomega.2c01494
43. S. Kourosh, F. Bayat, A. Shahrokhi, A. Baradaran, E. Yousefi, M. Mashreghi, A. Es-Haghi, M.E.T. Yazdi, Biomimetic synthesis and characterisation of homogenouse gold nanoparticles and estimation of its cytotoxity against breast cancer cell line. Mater. Technol. **37**(13), 2853–2860 (2022). https://doi.org/10.1080/10667857.2022.2081287
44. T. Yazdi, M. Ehsan, M.S. Amiri, F. Nourbakhsh, M. Rahnama, F. Forouzanfar, S.H. Mousavi, Bio-indicators in cadmium toxicity: role of HSP27 and HSP70. Environ. Sci. Pollut. Res. **28**, 26359–26379 (2021). https://doi.org/10.1007/s11356-021-13687-y
45. A.A. Noser, I.A. Shehadi, A.H. Abdelmonsef, M.M. Salem, Newly synthesized pyrazolinone chalcones as anticancer agents via inhibiting the PI3K/Akt/ERK1/2 signaling pathway. ACS Omega **7**, 25265–25277 (2022). https://doi.org/10.1021/acsomega.2c02181
46. M.M. El-Keiy, A.M. Radwan, T.M. Mohamed, Cytotoxic effect of soy bean saponin against colon Cancer. J. Biosci. Med. **7**, 70–86 (2019). https://doi.org/10.4236/jbm.2019.77006
47. J. Chen, X. Li, X. Zhao, Q. Wu, H. Zhu, Z. Mao, C. Gao, Doxorubicin-conjugated pH-responsive gold nanorods for combined photothermal therapy and chemotherapy of cancer. Bioact. Mater. **3**, 347–354 (2018). https://doi.org/10.1016/j.bioactmat.2018.05.003
48. J. Qin, Z. Peng, B. Li, K. Ye, Y. Zhang, F. Yuan, X. Yang, L. Huang, J. Hu, X. Lu, Gold nanorods as a theranostic platform for in vitro and in vivo imaging and photothermal therapy of inflammatory macrophages. Nanoscale **7**, 13991–14001 (2015). https://doi.org/10.1039/C5NR02521D